Data-driven approach for predicting abnormal grain growth in sintered binder jet steels

Mingzhang Yang[1], Mohsen K. Keshavarz[1], Mihaela Vlasea[1,*]

[1] Multi-scale Additive Manufacturing Laboratory, University of Waterloo, Waterloo, Ontario, N2M 3S1, Canada

* mihaela.vlasea@uwaterloo.ca

Abstract: Austenitic 316 stainless steel printed by binder jetting requires sintering to high densities to minimize porosity and have the corrosion resistance and strength required for most applications. While sintering can achieve densities above 99%, this paper reports the occurrence of abnormal grain growth (AGG) in this high-density region. A comprehensive process map is proposed, integrating key parameters to predict and inform grain sizes using regression model and machine learning approaches. Additionally, a clear relationship is identified between surface roughness, density, and grain size, offering a potential strategy for quality monitoring in serial production.

Keywords: Binder jet and sintering, stainless steel, machine learning, optimization, quality control

1. Introduction

Binder jetting additive manufacturing (BJAM) has gained traction for its ability to produce complex geometries at low unit cost, with austenitic 316 stainless steel (SS316) being one of the most widely adopted materials due to its robustness in corrosion resistance and mechanical properties [1]. To date, research on BJAM SS316 has largely focused on optimizing printing and sintering parameters for higher density, reducing distortion, improving mechanical properties, and understanding microstructure-property relationships [2,3]. Despite these advancements, there is no clear consensus on what defines high-quality sintered steels in BJAM, though it is generally accepted that key factors include good surface finish, maximum density, and minimal distortion. However, beyond these quality factors, the microstructure plays a critical role in determining the in-service performance of the final parts, with finer grains and uniform distribution being favorable for higher strength and fatigue performance [4]. In this context, there has been limited investigation into the evolution of grain structure during sintering.

Improper control of sintering can lead to undesirable microstructures that are often undetectable without destructive testing, making this a significant challenge in serial production. As such, the research objectives proposed in this work are twofold: (i) to examine the relationship between grain structure, surface finish, density, and sintering temperature in SS316; and (ii) based on these datasets, to create a comprehensive process map that serves as a practical tool for selecting optimal sintering temperatures to achieve the desired microstructure during production. To address the research objectives, we explored the grain size distribution of BJAM SS316 sintered to densities ranging from 90% to ~100%. A sintering map was proposed, integrating surface finish, density, and temperature to predict grain size and guide optimal sintering conditions.

2. Materials and methods

Gas-atomized SS316L powders with a D_{90} of 45 μm (Sandvik Osprey) were used. The nominal composition of the powders falls within ASTM A240 standard. The solidus temperature was calculated to be 1397°C using ThermoCalc (TCFE9 database). 1 cm^3 cuboidal samples were printed using a BJAM system (M-Flex, ExOne) with 100 μm layer thickness, 10 mm/s recoating speed, 300 rpm roller speed, 1800 rpm oscillator speed, and 40% binder saturation. After printing, the samples were cured at 180°C (12 h) in a curing oven (CT-333, JPW) under Ar. Afterward, specimens were debinded and sintered in a tube furnace (GSL-1600X, MTI) under a 5% H_2-95% Ar. The debinding was conducted at 400°C (2 h), while sintering entailed a ramp of 3°C/min up to temperatures between 1395°C and 1410°C (2 h hold), in increments of 1°C.

The sintered steels were characterized for their Archimedes density and topography of top surfaces using a 3D confocal microscope (VK-X250, Keyence). From surface images, the following three features are extracted: arithmetic mean height (S_a), maximum height of profile (S_z), and mean peak curvature (S_{pc}). Their definitions are detailed in ISO 25178-2:2021. The grains were revealed by standard metallographic preparations including vibration polishing (Buehler, VibroMet2). Imaging was conducted with a digital microscope (VHX-700, Keyence). Measurements of grain size were undertaken with the ImageJ which detects grain boundaries based on color contrast of binary images. All grain shapes were considered with the spherical equivalent diameter regarded as the grain size. At least 300 grains were measured for

each sample. Microstructure was analyzed using a scanning electron microscopy (SEM) (Vega3, Tescan) with an electron backscatter diffraction (EBSD) detector.

3. Results and discussion

Figures 1(a-d) display the representative top skin surface maps of sintered parts within the narrowed temperature window of 1395 -1410°C. At 1395°C, the surface was rough with distinct bumps from individual powder particles. At 1400°C, these bumps begin to coalesce. By 1405°C, the surface smoothens, though some particle agglomeration remains. At 1410°C, the surface was further refined, with minimal agglomeration. Quantitatively, S_a, S_z, and S_{pc} values were plotted against the measured relative density and presented in Figure 1(e). The sintering window enabled densification from approximately 90% to 100%, accompanied by a reduction in all surface texture parameters. Notably, there was a change in the rate of reduction around 98.5% density, which may correspond to a shift in dominant sintering mechanisms. A similar trend was observed during the sintering of low-alloy steels in our previous work [5,6].

Higher sintering temperatures can promote densification by allowing grains to migrate and coarsen via the Ostwald ripening [7]. This usually results in fewer, larger grains. However, the distributions shown in Figure 2(a-b) reveal an opposite trend. The steel sintered at the higher temperature (1410°C) exhibited higher fraction of finer grains compared to that of 1400°C, indicating a form of grain refinement. Additionally, a few exceptionally large grains (>150 µm) were observed, suggesting abnormal grain growth [8]. The fine grains observed under both conditions predominantly originate from the statistically finer-sized δ-ferrite phase, with the 1410°C sample showing a noticeably higher area fraction of δ-ferrite. Several instances of tiny, stray grains with different orientations from the surrounding grains are highlighted by the yellow circles in Figure 2. Additionally, fine γ-austenite grains, occasionally enclosed by δ-ferrite also contribute to the fine grain size distribution.

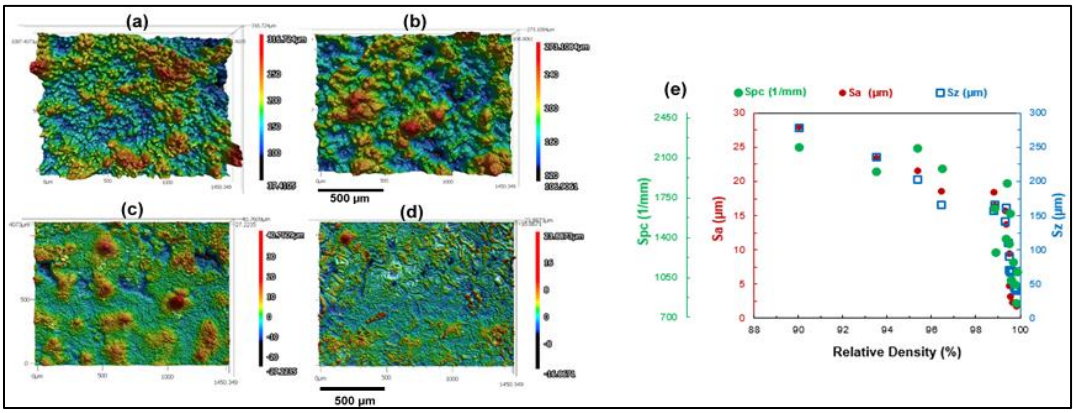

Figure 1. Surface height maps of the SS316 L steels sintered from (a) 1395°C, (b) 1400°C, (c) 1405°C, and (c) 1410°C. (e) Relationship between S_a, S_z, and S_{pc} and relative density.

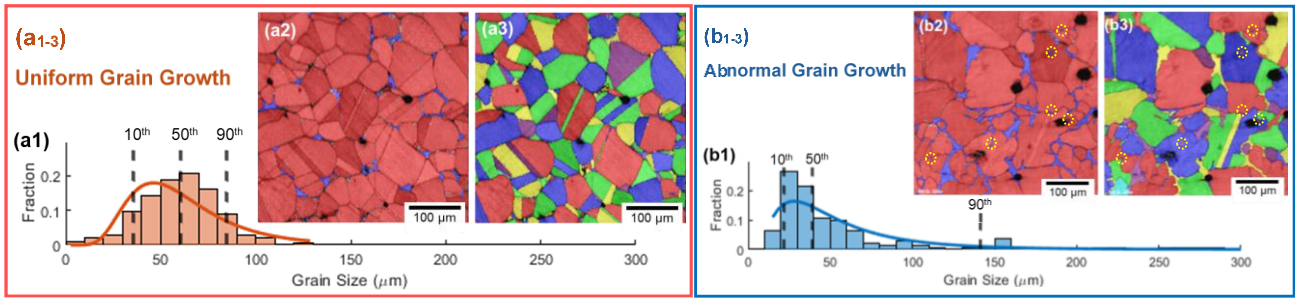

Figure 2. (a1, b1) Grain size distribution with log-normal fits to the data (solid line); (a2, b2) EBSD phase map, where blue indicates δ-ferrite and red represents γ-austenite, and (a3, b3) grain boundary maps for the SS316L sintered from 1400°C and 1410°C, respectively.

Heterogeneous microstructures with abnormally large grains can degrade mechanical properties like fatigue and fracture toughness. Traditional sintering optimization in BJAM is based on temperature and density, often overlooking these microstructural anomalies. Hence, to better capture the material's physical behavior, we extracted the 10th (D_{10}), 50th (D_{50}), and 90th percentiles (D_{90}) of the grain size distribution for all sintered steel samples and plotted them against

density, S_a, and sintering temperature (Figure 3(a-c)). Samples sintered to above ~99% density show abnormally large grains (Figure 3(c)), with the D_{90} grain size exceeding 120 µm. These samples also contain exceptionally fine grains, with the D_{10} (< 25 µm) even finer than those sintered at the lowest temperature of 1395°C (Figure 3(a)). This significant variance in grain size distribution, along with its high sensitivity to temperature, makes the quality assurance of the final parts difficult in the presence of potential temperature fluctuations.

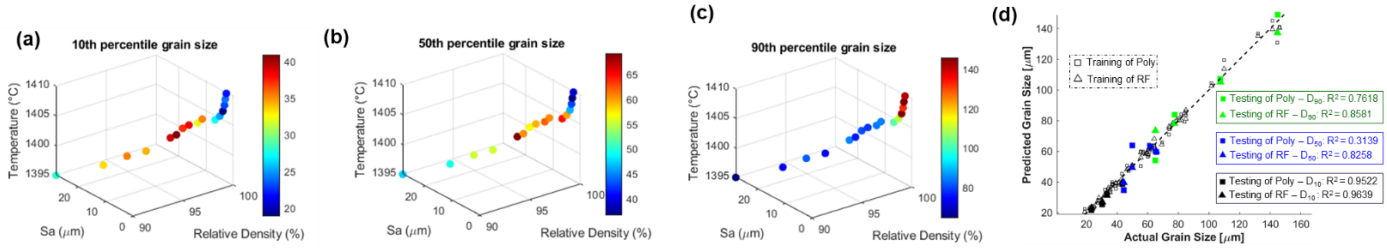

Figure 3. (a) D_{10}, (b) D_{50}, and (c) D_{90} grain sizes plotted as a function of relative density, S_a roughness, and temperature, with the color bar representing grain size values. (d) Predicted vs actual grain sizes using regression and RF models, along with R^2 values from test data.

Specifically, during batch production in the same furnace, temperature deviation from the set point can occur due to factors such as thermocouple placement, sample positioning, or gas flow, leading to undesirable microstructures such as the abnormal grain growth observed here. To mitigate this, incorporating surface roughness and/or density as supplementary indicators of grain size can reduce variability compared to a model based solely on set temperatures. Therefore, we attempted both polynomial regression[1] and random forest (RF)[2] models to fit grain size data (D_{10}, D_{50}, D_{90}) using temperature, S_a, and relative density as inputs. Figure 3(d) shows the data fitting for both models. The simple polynomial model achieves R^2 values above 0.88, indicating a clear relationship. However, on an independent test dataset, only the RF model maintained strong performance, with R^2 values of 0.83, 0.86, and 0.96 for D_{10}, D_{50}, and D_{90}, respectively. Although machine learning models like RF are prone to overfitting without hyperparameter tuning, this risk is minimized here because the model will only be applied within the defined sintering temperature range (1395°C-1410°C) required to achieve over 90% density. Within this range, each temperature correlates with a specific set of Sa roughness and density values, which are indicative of the resulting grain size. To further showcase the predictive capabilities of the sintering map, a Bayesian optimization algorithm[3] was coupled with the RF model to perform an inverse design, searching for the optimal temperature that yields a targeted microstructure. To monitor AGG, the objective function in this optimization process was defined to minimize the difference between the predicted and desired grain size variance (where variance = $D_{90}-D_{10}$). The desired variances were set to 40, 60, 80, 100, and 120 µm for illustration. The results, displayed through their respective objective function models (Figure 4 (a-e)), demonstrated high accuracy, with the optimal temperatures closely matching the actual temperatures (Figure 4 (f)). This approach highlights the potential for precise grain structure control in serial production.

4. Conclusion

This study systematically evaluated the sintering behavior of SS316L in terms of density, surface quality, and grain structure. While sintering enabled densification from 90% to nearly 100%, it was discovered that abnormal grain growth can occur in this widely used BJAM material in high-density regions (> 99%). This phenomenon led to the formation of ultra-large grains (> 120 µm) alongside fine grains (< 25 µm), resulting in a heterogeneous microstructure. To prevent abnormal grain growth, the study proposes a processing map integrating density, surface roughness, and temperature. This map supports the modeling of grain sizes using regression models or machine learning, facilitating the inverse design of sintering temperatures to mitigate abnormal grain growth. Additionally, this study demonstrates that using readily accessible surface features to infer microstructure is a promising pathway for quality control in serial production.

[1] The polynomial regression model used in this study is a second-degree polynomial model, incorporating interaction and squared terms of the three input features.

[2] Random forest is a decision tree machine learning algorithm to model complex, nonlinear relationships, given the limited data. The model was trained with 30 trees, using a minimum leaf size of 2 and a maximum of 30 splits.

[3] Bayesian optimization developed in this work used the random forest model as the surrogate function. The surrogate function provided a probabilistic approximation of the unknown objective function based on prior evaluations, using Gaussian process regression by default.

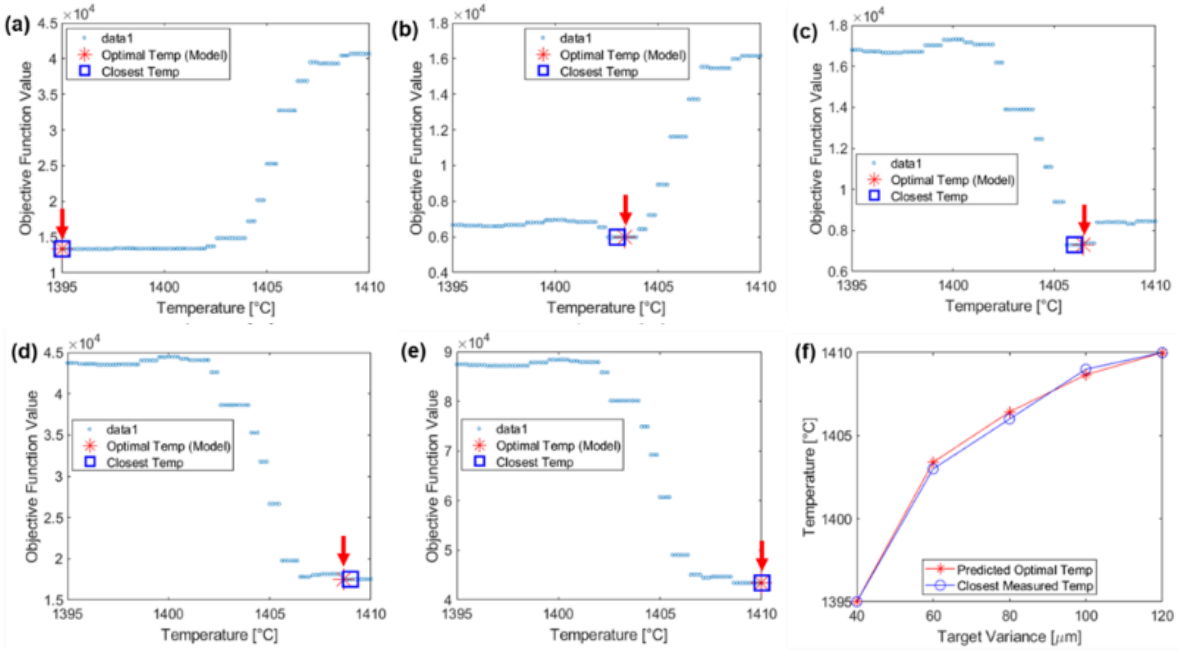

Figure 4. Optimal sintering temperature prediction using Bayesian optimization: (a-e) objective function models for target grain size variances of 40, 60, 80, 100, and 120 µm; (f) comparison of predicted optimal temperatures with closest matching measured temperatures.

5. Acknowledgments

The authors appreciate the funding support received from the Natural Sciences and Engineering Research Council of Canada (NSERC), grant ALLRP 580559 – 22.

6. Conflicts of interest

The authors confirm no financial or personal relationships that could influence the current research.

7. References

[1] A. Mostafaei et al., “Binder jet 3D printing—Process parameters, materials, properties, modeling, and challenges,” Prog. Mater. Sci., vol. 119, no. June 2020, p. 100707, 2021, doi: 10.1016/j.pmatsci.2020.100707.

[2] M. Jamalkhani, B. Nathan, M. Heim, D. Nelson, and A. Mostafaei, “Fatigue behavior of vacuum-sintered binder jetted fine 316L stainless steel powder,” Mater. Sci. Eng. A, vol. 873, no. March, p. 144937, 2023, doi: 10.1016/j.msea.2023.144937.

[3] S. Mirzababaei, B. K. Paul, and S. Pasebani, “Microstructure-property relationship in binder jet produced and vacuum sintered 316 L,” Addit. Manuf., vol. 53, no. December 2021, p. 102720, 2022, doi: 10.1016/j.addma.2022.102720.

[4] P. Kumar, R. Jayaraj, J. Suryawanshi, U. R. Satwik, J. McKinnell, and U. Ramamurty, “Fatigue strength of additively manufactured 316L austenitic stainless steel,” Acta Mater., vol. 199, pp. 225–239, 2020, doi: 10.1016/j.actamat.2020.08.033.

[5] M. Yang, J. Yan, P. Peng, P. D. Enrique, M. K. Keshavarz, and M. Vlasea, “Surface functionalization of binder jetted steels through super-solidus liquid phase sintering and electro-spark deposition,” Surf. Coatings Technol., vol. 487, no. June, p. 130994, 2024, doi: 10.1016/j.surfcoat.2024.130994.

[6] M. Yang, M. K. Keshavarz, M. Vlasea, and A. Molavi-kakhki, “Towards full-dense high geometric fidelity parts via binder jetting and controlled sintering,” J. Manuf. Process., vol. 115, no. December 2023, pp. 180–191, 2024, doi: 10.1016/j.jmapro.2024.02.028.

[7] M. Yang, M. K. Keshavarz, M. L. Vlasea, A. Molavi-Kakhki, and L. Martin, “Supersolidus Liquid Phase Sintering of Water-Atomized Low-Alloy Steel in Binder Jetting Additive Manufacturing,” Heliyon, vol. 9, no. 3, p. e13882, 2023, doi: 10.2139/ssrn.4283080.

[8] R. M. German, “Coarsening in Sintering : Grain Shape Distribution , Grain Size Distribution , and Grain Growth Kinetics in Solid-Pore Systems Coarsening in Sintering : Grain Shape Distribution , Grain Size Distribut,” Crit. Rev. Solid State Mater. Sci., vol. 8436, 2010, doi: 10.1080/10408436.2010.525197.